

**Localized states with nontrivial symmetries: Localized labyrinthine patterns**M. G. Clerc<sup>1</sup>, S. Echeverría-Alar<sup>1</sup>, and M. Tlidi<sup>2</sup><sup>1</sup>*Departamento de Física and Millennium Institute for Research in Optics, FCFM, Universidad de Chile, Casilla 487-3, Santiago, Chile*<sup>2</sup>*Faculté des Sciences, Université libre de Bruxelles (U.L.B), CP. 231, 1050 Brussels, Belgium*

(Received 8 April 2021; revised 25 July 2021; accepted 11 January 2022; published 28 January 2022)

The formation of self-organized patterns and localized states are ubiquitous in Nature. Localized states containing trivial symmetries such as stripes, hexagons, or squares have been profusely studied. Disordered patterns with nontrivial symmetries such as labyrinthine patterns are observed in different physical contexts. Here we report stable localized disordered patterns in spatially extended dissipative systems. These two- and three-dimensional localized structures consist of an isolated labyrinth embedded in a homogeneous steady state. Their partial bifurcation diagram allows us to explain this phenomenon as a manifestation of a pinning-depinning transition. We illustrate our findings on the Swift-Hohenberg-type of equations and other well-established models for plant ecology, nonlinear optics, and reaction-diffusion systems.

DOI: [10.1103/PhysRevE.105.L012202](https://doi.org/10.1103/PhysRevE.105.L012202)

Spatiotemporal patterning resulting from a symmetry-breaking instability is a central issue in almost all driven far from equilibrium systems [1–3]. Localized structures, dissipative solitons, and localized patterns belong to this field of research. They consist of one or more regions in one state surrounded by a region in a qualitatively different state [4–8]. Spatial localization appears not only in nonlinear systems, but can occur in linear ones such as Anderson localization that arises in inhomogeneous systems [9]. Localized states appear in other classes of experimentally relevant systems such as nonlinear optics and photonics. Spatial localized patterns possess potential applications to all-optical control of light, optical storage, and information processing [6,8].

Localized patterns involving trivial symmetries such as stripes, hexagons, or squares have been abundantly discussed and are by now fairly well understood, including their respective snaking bifurcation diagrams [7,10]. Indeed, these localized patterns involve few Fourier modes. However, localized patterns with nontrivial symmetries have neither been experimentally observed nor documented, nor theoretically predicted. An example of this type of patterning phenomenon is referred to as localized labyrinthine patterns (LLP). They are observed in population biology, such as in vegetation populations, on the skin of animals, or human bodies [cf. Fig. 1]. All these examples show an area, which is not necessarily circular, containing complex spatial structures, a labyrinth, and surrounded by a uniform state. In the vegetation populations, this intriguing phenomenon seems to be stationary (see the Supplementary Material [20]). Extended labyrinthine patterns refer to two-dimensional (2D) or more-dimensional dissipative structures characterized by a circular or spherical powder-like spectrum globally [12], they exhibit a short-range order with a single Fourier mode, and have a finite number of defects [13]. A power spectrum with a powdered ring (sphere)

structure is the main characteristic of patterns with nontrivial symmetries.

In this Letter, we account for the formation of localized patterns with nontrivial symmetries in well-established models from ecology, optics, and reaction-diffusion systems. We illustrate and investigate this phenomenon using a Swift-Hohenberg equation (SHE) [14], which constitutes a well-known paradigm in the study of spatial periodic or localized patterns in spatially extended systems [2]. We show that this model supports static and stable LLP. Considering adequate initial conditions, LLP are generated in the coexistence region between the extended labyrinth and homogenous state. We draw the partial bifurcation diagram showing the stability domain of LLP and their pinning-depinning transitions, where the localized labyrinth exists as a stationary solution. Free energy allows us to study the relative stability analysis. We show numerical evidence of stable three-dimensional localized labyrinthine patterns. Further, within the pinning range of parameters, three LLP with different sizes are generated for a fixed value of the system parameters.

The SHE reads ([14])

$$\partial_t u = \epsilon u - u^3 - \nu \nabla^2 u - \nabla^4 u, \quad (1)$$

where the real order parameter  $u = u(x, y, z, t)$  is an excess scalar field variable measuring the deviation from criticality,  $\epsilon$  is the control parameter, and  $\nu$  the (anti) diffusion coefficient for (positive) negative value. The cubic term accounts for the nonlinear response of the system under study. The Laplace operator  $\nabla^2 = \partial_{xx} + \partial_{yy} + \partial_{zz}$  acts in the  $(x, y, z)$ -Euclidean space and  $t$  is time. The last term on the right-hand side, the bi-Laplacian, stands for hyperdiffusion. Equation (1) can also be used to describe 2D systems, where the Laplacian, bi-Laplacian, and the order parameter  $u$  are defined in the  $(x, y)$ -Euclidean space. The model equation (1) can be rewritten in a variational form as  $\partial_t u = -\delta \mathcal{F} / \delta u$ , where  $\mathcal{F}$  is a

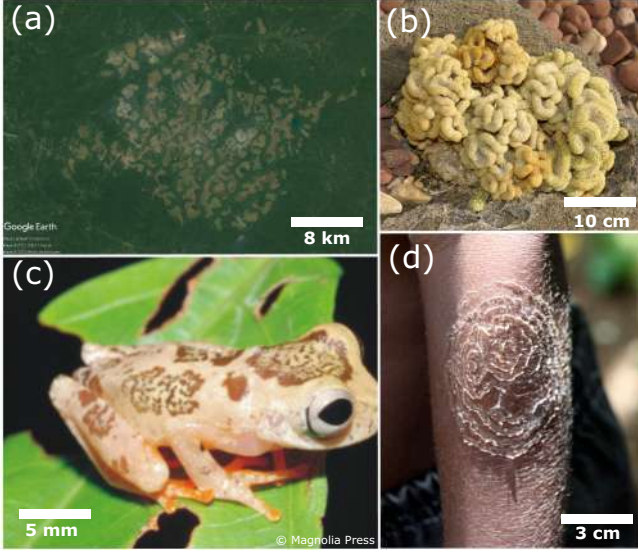


FIG. 1. Snapshots of localized labyrinthine patterns in natural systems. (a) Irregular distribution of vegetation embedded in a uniform vegetated cover observed in central Cameroon using Google Earth software (with ground coordinate  $3^{\circ}58'22.70''$  N  $12^{\circ}19'05.84''$  E). (b) Brain cactus (*Mammillaria Elongata Cristata*) with a contorted tissue (courtesy of David Stang). It is a localized structure in the bare soil background. (c) Pigmented areas composed of stripes and spots in the skin dorsum of a frog (*Dendropsophus ozzyi*) [11] (reproduced with permission from the copyright holder). (d) Skin lesions of *Tinea imbricata* disease (courtesy of Michael Marks).

Lyapunov functional or a free energy

$$\mathcal{F} = \int \frac{dx dy dz}{2} \left( -\epsilon u^2 + \frac{u^4}{2} - v(\nabla u)^2 + (\nabla^2 u)^2 \right). \quad (2)$$

The variational structure of the SHE (1) indicates that only stationary solutions such as uniform states, spatially periodic, or localized patterns are possible. The SHE (1) is a well-known paradigm for the study of periodic and localized patterns, was first derived in hydrodynamics [14], and later in other fields of natural science, such as chemistry [15], and nonlinear optics [16]. In the last decade, it has been established that Eq. (1) has already been constructed by Turing, but was unpublished [17].

Other real SHE was derived for out of equilibrium systems [18,19]

$$\partial_t u = \eta - \epsilon u - u^3 - (v - bu)\nabla^2 u - \nabla^4 u - c(\nabla u)^2, \quad (3)$$

where  $\epsilon$  and  $\eta$  are control parameters;  $v$ ,  $b$  are diffusion parameters; and  $c$  is the nonlinear advection strength. The presence of nonlinear diffusion and nonlinear advection terms,  $u\nabla^2 u$  and  $(\nabla u)^2$ , render Eq. (3) nonvariational. In general, this equation does not admit a Lyapunov functional.

Whether a SHE model is variational or not, numerical simulations of both models, Eqs. (1) and (3) with periodic boundary conditions show evidence of stable stationary localized labyrinthine patterns [see Figs. 2(a) and 2(b)].

To obtain localized labyrinthine patterns, the initial conditions consist of a circular area, of certain diameter  $d$ , of a stable labyrinthine pattern in the center of the simulation box, embedded in a uniform background. The evolution towards

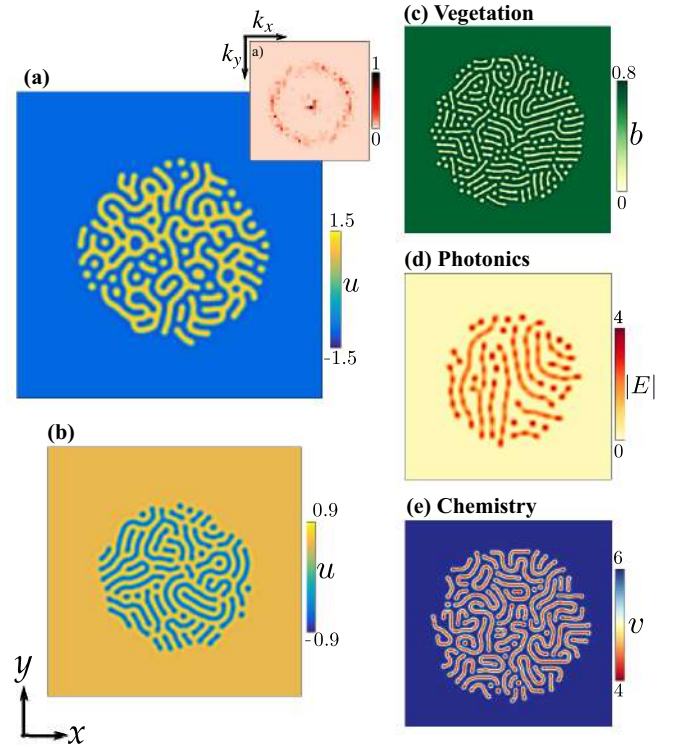


FIG. 2. Stationary localized labyrinthine patterns obtained in different pattern forming models: (a) SHE (1) ( $\epsilon = 1.17$ ,  $v = 1$ ); (b) generalized SHE (3) ( $\epsilon = 0.2$ ,  $v = 1$ ,  $\eta = -0.06$ ,  $b = 0.1$ ,  $c = 0.1$ ); (c) nonlocal vegetation; (d) passive diffractive resonator; and (e) reaction-diffusion. See the Supplementary Material for more details of models and parameters used in (c), (d), and (e) [20]. The right-upper inset in (a) shows the powder-like ring spectrum of the LLP in the SHE model (1). All the localized structures fulfill the definition of labyrinthine patterns (see Supplementary Material [20] for details).

equilibrium starts with a quick adjustment of the interface mediated by the curvature of the stripe patterns; then there is an accommodation of the stripe patterns in the bulk. To this end, some retraction of stripes in the interface takes place (cf. Video 1 and the stabilization of LLP in the Supplementary Material [20]). The final localized region is not perfectly circular, containing finite segments of deformed stripes separated by spots of the same width, and a high number of defects inherited from the extended labyrinth. These finite-size stripes can be interconnected or not. They support all stripe orientations along the motionless interface separating the labyrinth to the homogeneous steady state, as shown in Fig. 2. Note that localized nontrivial symmetry patterns arise between the critical sizes  $d_o \leq d \leq d_c$  (see the Supplementary Material [20] for details). In addition, the formation of LLP in the above scalar model equations in the form of SHE, additional models are also considered that are experimentally relevant. First, a generic interaction redistribution model describing vegetation pattern formation which is an integrodifferential model equation. This simple modeling approach based on the interplay between short-range and long-range interactions governing plant communities captures localized labyrinthine pattern as shown in Fig. 2(c). Second, broad area photonics devices such as nonlinear resonators subjected to a coherent injected

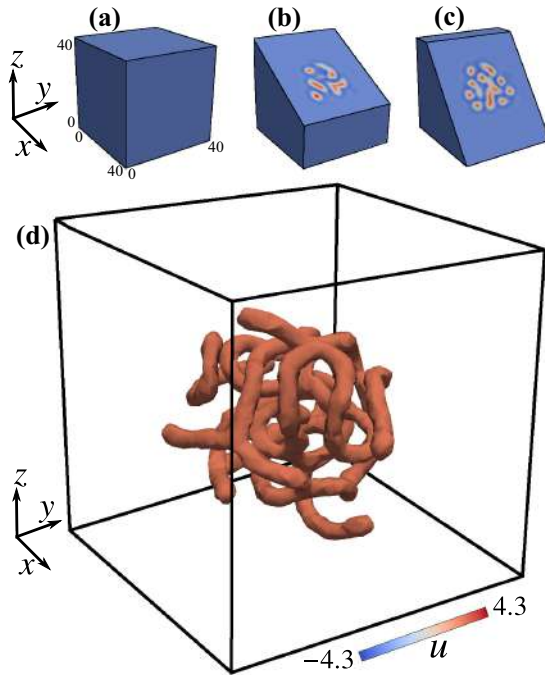


FIG. 3. Three-dimensional localized labyrinthine pattern solution of Eq. (3). (a) Color map of the full simulation, (b) and (c) are color map slices of the localized labyrinthine pattern. (d) Isosurface of the localized labyrinthine pattern with  $u = 1.3$ . Parameters are  $\epsilon = 4.2$ ,  $\nu = 5$ ,  $\eta = -6.8$ ,  $b = 0$ , and  $c = 0$ . The mesh integration is  $40 \times 40 \times 40$ .

beam [see Fig. 2(d)]. In this case, the resulting equation is a complex Ginzburg-Landau-type equation. Finally, a reaction-diffusion model for chemical dynamics, also supports LLP as shown in Fig. 2(e). The description of these models and the values of the parameters are provided in the Supplementary Materials [20]. Similar solutions when using Dirichlet and Neumann boundary conditions are observed. Also, localized labyrinthine patterns are independent of the numerical grid size (see the Supplementary Material [20] for details).

The 2D LLP are robust structures in 2D systems in the various natural system, that is, this phenomenon is observed in different physical systems as shown in Fig. 1 and in the Supplementary Material [20]. It has been shown that the Swift-Hohenberg equation supports three-dimensional (3D) extended patterns with trivial symmetries such as lamellae, body-centered cubic crystals, hexagonally packet cylinders [25–28], and localized patterns [27–29]. Recently, clusters of 3D bullets forming a localized crystal with trivial symmetry were reported [30]. We extend this analysis to 3D nontrivial symmetry patterns and we show the existence of stable 3D localized labyrinthine patterns. They consist of finite-size curved and connected tubes embedded in a homogeneous background. The width of the tubes is half of the critical wavelength at the symmetry-breaking instability. They are obtained by numerical simulations of the generalized SHE Eq. (3) with Neumann boundary conditions along  $x$ ,  $y$ , and  $z$  directions. Figure 3 shows a typical 3D localized labyrinthine pattern.

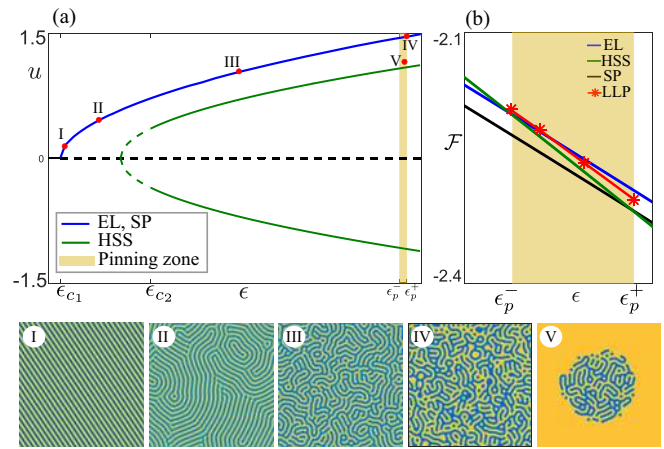


FIG. 4. (a) Bifurcation diagram of homogeneous solutions and (b) relative stability analysis of a localized labyrinth in SHE (1) with  $\nu = 1$ . The uniform  $u(x, y) = 0$  state suffers a Turing instability at  $\epsilon_{c1} = -0.25$ . The uppermost curve (blue) shows the maximum  $u(x, y)$  of the different equilibrium patterns [stripe (i), fingerprint-type labyrinth (ii), glassy labyrinth (iii), and scurfy labyrinth (iv)]. At  $\epsilon_{c2} = 0.125$ , the nonzero homogeneous states (HSS-green curves) are unstable to in-homogeneous perturbations. In the narrow region limited by  $\epsilon_p^- = 1.16$  and  $\epsilon_p^+ = 1.19$ , where the extended labyrinthine pattern and the uniform solutions coexist, the existence of localized labyrinthine patterns (v) is possible. Free energy  $\mathcal{F}$  given by Eq. (2) is computed for an extended labyrinth (EL), the stripe pattern (SP), the homogeneous states (HSS), and a localized labyrinthine pattern (LLP) near the pinning region.

The homogeneous steady states  $u_s = 0$  and  $u_{s\pm} = \pm\epsilon^{1/2}$  solutions of Eq. (1) undergo symmetry-breaking instabilities at  $\epsilon_{c1} = -\nu^2/4$  and  $\epsilon_{c2} = \nu^2/8$ . At both critical bifurcation points the critical wavelength is  $\lambda_c = 2\pi/k_c = 2\sqrt{2\pi}/\sqrt{\nu}$ . Indeed, when the linear coefficient of the Laplacian is negative  $\nu > 0$ , the spontaneous pattern formation process becomes possible thanks to the appearance of a finite band of linearly unstable Fourier modes that triggers the appearance of spatially periodic patterns. The upper cutoff is affected by the bi-Laplacian term, which is always stabilizing for short distances since dispersion is an efficient mixing mechanism. Numerical simulations of the bi-dimensional Eq. (1) in the neighborhood of the critical point  $\epsilon = \epsilon_{c1}$  indicate the emergence of extended patterns, as shown in Fig. 4(a). When increasing the control parameter, the sequence of symmetry-breaking transitions fingerprint, glassy, and scurfy labyrinthine patterns are observed [13].

Spatial confinement leading to the formation of localized patterns with nontrivial symmetry occurs in parameter space ( $\epsilon > \epsilon_{c2}$ ), where extended labyrinthine patterns coexist with a homogeneous steady state. Within this hysteresis loop, there generally exists a so-called pinning range of parameters [31], delimited by  $\epsilon_p^\pm$ , in which LLP can be observed [cf. Fig. 4(a)]. Taking advantage of the variational structure of Eq. (1), we address the problem of the relative stability analysis. We evaluate numerically  $\mathcal{F}$ , associated with uniform states, extended labyrinth, and LLP. Figure 4(b) summarizes the results. These equilibria correspond to a local or global minimum of Lyapunov functional  $\mathcal{F}$  given by Eq. (2). From Fig. 4(b),

we see that the localized labyrinth is more energetically favorable than the extended labyrinth (EL) but less stable than the homogeneous steady state (HSS) and the perfect stripe pattern (SP). The limiting points of the stability region of the localized labyrinth solutions  $\epsilon_p^- < \epsilon < \epsilon_p^+$  are similar to the  $\epsilon$  parameters associated to the interchange of metastability between extended states. The localized labyrinths are stationary and stable patterns since their localized area never expands despite diffusion and never shrinks despite nonlinearity and dissipation.

Localized patterns with trivial symmetry (stripes and hexagons) are organized into a complex diagram following a homoclinic snaking bifurcation [7]. This type of diagram is obtained by a continuation method. The symmetries of the localized structures are relevant for the convergence of this algorithm. However, in the case of LLP there is a lack of continuation algorithms to characterize the full bifurcation diagram. To figure out the existence region of stable LLP, we performed direct numerical simulations of Eq. (1). Figure 5(a) summarizes the results, where we plot

$$\|u\|^2 = \frac{1}{L_x L_y} \int_0^{L_x} \int_0^{L_y} [u(x, y) - u_{s+}]^2 dx dy, \quad (4)$$

as a function of the bifurcation parameter. The full bifurcation diagram can be complex, so we display only three branches of LLP obtained with different initial conditions shown in the insets (i), (ii), and (iii) of Fig. 5(a). The maximum amplitude of the three LLPs is the same, but they have different sizes. Varying  $\epsilon$  from these initial conditions, we obtain the three branches shown in Fig. 5(a). Whatever the initial condition, when increasing the bifurcation parameter the LLP decrease in size, mediated by the shrinking of fingers and accommodation of defects (see the Supplementary Material [20] for details). All LLP disappear close to  $\epsilon > \epsilon_p^+$  and the system exhibit a transition towards a mixture of circular localized peaks and dips. Figure 5(b) illustrates this transition, during which we observe the contraction of fingers, which transform to circular peaks or dips. This process correspond to the inverse of the invagination of localized structures [32]. Starting from the initial conditions shown in the insets (i), (ii), and (iii) of Fig. 5(a) and decreasing the bifurcation parameter, we observe an increase in the size of the LLP. Further decreasing  $\epsilon < \epsilon_p^-$ , we observe a transition to an extended fingerprint-like labyrinthine pattern. This depinning transition mediated by front propagation has the tendency to reduce the number of circular spots and dips, and enhance the invagination process as illustrated in Fig. 5(c).

By varying the control parameter within the pinning region delimited by  $\epsilon_p^-$  and  $\epsilon_p^+$ , we see that for a fixed  $\epsilon$ , and near  $\epsilon = \epsilon_p^-$  the sizes of the coexisting LLP are different. However, close to  $\epsilon = \epsilon_p^+$  the system reaches more or less the same size. We stress that the position of LLP and their size depends on the initial conditions, and the maximum of the coexisting LLP is essentially constant for fixed values of the system parameters. The number of coexisting LLP with different sizes can be much larger than the three branches shown in the bifurcation diagram displayed in Fig. 5(a).

The localized patterns with trivial symmetries have a well-established bifurcation diagram based on continuation

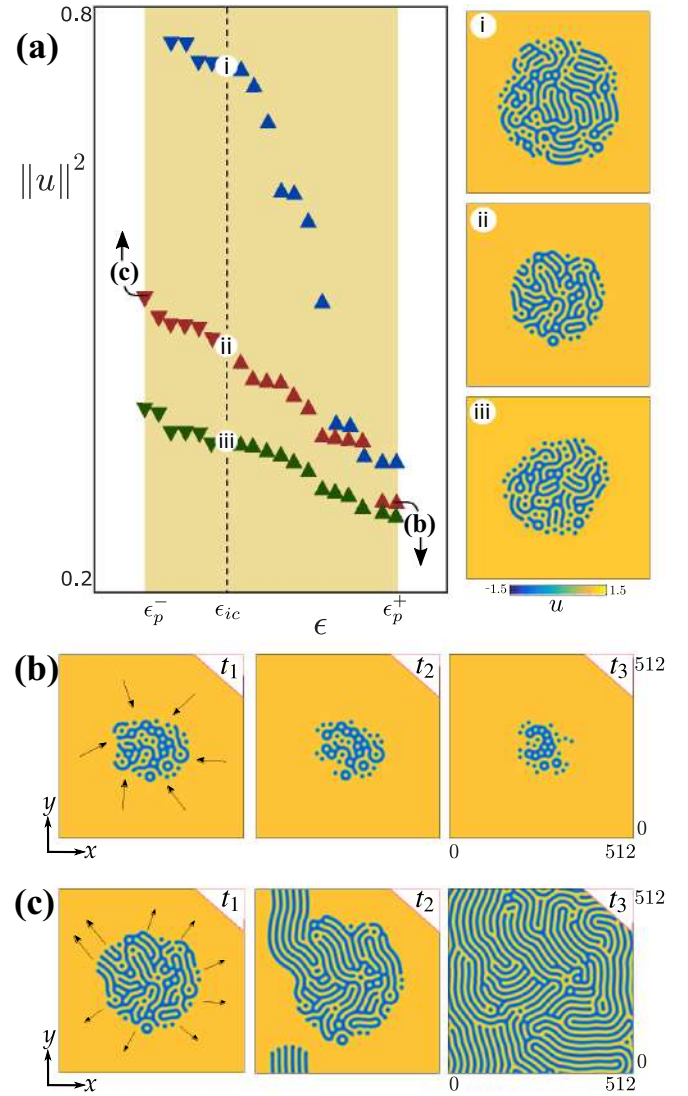


FIG. 5. Three stable branches of LLP and pinning-depinning transitions in the SHE model (1). (a) Plot of  $\|u\|^2$  for three initial conditions (i, ii, and iii) with different sizes (see Fig. 3 in the Supplementary Material [20] for details). The upward (downward) triangles account for the increasing (decreasing) of  $\epsilon$ , starting from  $\epsilon_{ic} = 1.17$ . (b) Temporal sequence of the pinning-depinning transition when crossing  $\epsilon_p^+ = 1.19$  and (c)  $\epsilon_p^- = 1.16$ .

methods. However, when dealing with localized patterns with nontrivial symmetries, there are no available algorithms for the continuation to handle this problem. Whether the localized labyrinthine patterns present a homoclinic snaking bifurcation diagram or not remains an open question. The plausibility of spatial varying parameters can be responsible for complex localized patterns. However, our result opens a novel possibility of localized patterns with nontrivial symmetries even in homogenous and isotropic systems. The existence of these types of localized patterns is the consequence of an intricate interplay between pinning, defects, and complex-shaped interface.

M.G.C. acknowledges the financial support of ANID–Millennium Science Initiative Program–ICN17\_012 (MIRO)

and FONDECYT project 1210353. S.E.-A. acknowledges the financial support of ANID by Beca Doctorado Nacional 2020-21201376. A part of this work was supported by the “Laboratoire Associé International” University of Lille, ULB

on “Self-organisation of light and extreme events” (LAI-ALLURE). M.T. acknowledges financial support from the Fonds de la Recherche Scientifique FNRS under Grant CDR No. 35333527 “Semiconductor optical comb generator.”

- [1] P. Glansdorff and I. Prigogine, *Thermodynamic Theory of Structure, Stability, and Fluctuations* (Wiley-Interscience, New York, 1971).
- [2] M. C. Cross and P. C. Hohenberg, Pattern formation outside of equilibrium, *Rev. Mod. Phys.* **65**, 851 (1993).
- [3] J. D. Murray, *Mathematical Biology: I. An Introduction*, (Springer Science & Business Media, New York, 2007).
- [4] O. Descalzi, M. Clerc, S. Residori, and G. Assanto, *Localized States in Physics: Solitons and Patterns* (Springer, New York, 2011).
- [5] H. G. Purwins, H. U. Bödeker, and Sh. Amiranashvili, Dissipative solitons, *Adv. Phys.* **59**, 485 (2010).
- [6] M. Tlidi, K. Staliunas, K. Panajotov, A. G. Vladimirov, and M. G. Clerc, Localized structures in dissipative media: From optics to plant ecology, *Phil. Trans. R. Soc. A* **372**, 20140101 (2014).
- [7] E. Knobloch, Spatial localization in dissipative systems, *Annu. Rev. Condens. Matter Phys.* **6**, 325 (2015).
- [8] L. Lugiato, F. Prati, and M. Brambilla, *Nonlinear Optical Systems* (Cambridge University Press, Cambridge, England, 2015).
- [9] P. W. Anderson, Absence of diffusion in certain random lattices, *Phys. Rev.* **109**, 1492 (1958).
- [10] P. Couillet, Localized patterns and fronts in nonequilibrium systems, *Int. J. Bifurcation Chaos Appl. Sci. Eng.* **12**, 2445 (2002).
- [11] V. G. D. Orrico, A new “Bat-Voiced” species *Dendrophosus* Fitzinger, 1843 (Anura, Hyliade) from the Amazon Basin, Brazil, *Zootaxa* **3881**, 4 (2014).
- [12] M. Le Berre, E. Ressayre, A. Tallet, Y. Pomeau, and L. Di Menza, Example of a chaotic crystal: The labyrinth, *Phys. Rev. E* **66**, 026203 (2002).
- [13] S. Echeverria-Alar and M. G. Clerc, Labyrinthine patterns transitions, *Phys. Rev. Research* **2**, 042036(R) (2020).
- [14] J. Swift and P. C. Hohenberg, Hydrodynamic fluctuations at the convective instability, *Phys. Rev. A* **15**, 319 (1977).
- [15] M.F. Hilali, G. Dewel, and P. Borckmans, Subharmonic and strong resonances through coupling with a zero mode, *Phys. Lett. A* **217**, 263 (1996).
- [16] M. Tlidi, P. Mandel, and R. Lefever, Localized Structures and Localized Patterns in Optical Bistability, *Phys. Rev. Lett.* **73**, 640 (1994).
- [17] J. H. Dawes, After 1952: The later development of Alan Turing’s ideas on the mathematics of pattern formation, *Hist. Math.* **43**, 49 (2016).
- [18] M. G. Clerc, A. Petrossian, and S. Residori, Bouncing localized structures in a liquid-crystal light-valve experiment, *Phys. Rev. E* **71**, 015205(R) (2005).
- [19] G. Kozyreff and M. Tlidi, Nonvariational real Swift-Hohenberg equation for biological, chemical, and optical systems, *Chaos* **17**, 037103 (2007).
- [20] See Supplemental Material at <http://link.aps.org/supplemental/10.1103/PhysRevE.105.L012202> for details on the complexity of localized labyrinthine patterns in the models described here [Eqs. (1) and (3)] and in [20] (vegetation, nonlinear optics, reaction-diffusion). Video 1 shows the stabilization process of a localized labyrinthine pattern in the SHE model 1. Discussion of critical size for LLP formation. Details on numerical simulations of LLP in the SHE model 1 with Neumann and Dirichlet boundary conditions and different grid sizes. The growth mechanism along one stable branch of LLP is described. The Supplemental Material includes the references [21–24].
- [21] M. Tlidi, R. Lefever, and A. Vladimirov, On vegetation clustering, localized bare soil spots and fairy circles, *Lect. Notes Phys.* **751**, 381 (2008).
- [22] J. von Hardenberg, E. Meron, M. Shachak, and Y. Zarmi, Diversity of Vegetation Patterns and Desertification, *Phys. Rev. Lett.* **87**, 198101 (2001).
- [23] M. Le Berre, E. Ressayre, and A. Tallet, Why does a Ginzburg-Landau diffraction equation become a diffusion equation in the passive ring cavity?, *Quantum Semiclass. Opt.* **7**, (1995).
- [24] E. C. Edblom, M. Orban, and I. R. Epstein, A new iodate oscillator: The Landolt reaction with ferrocyanide in a CSTR, *J. Am. Chem. Soc.* **108**, 2826 (1986).
- [25] U. Thiele, A. J. Archer, M. J. Robbins, H. Gomez, and E. Knobloch, Localized states in the conserved Swift-Hohenberg equation with cubic nonlinearity, *Phys. Rev. E* **87**, 042915 (2013).
- [26] H. G. Lee, A semi-analytical Fourier spectral method for the Swift-Hohenberg equation, *Comput. Math. Appl.* **74**, 1885 (2017).
- [27] K. Staliunas, Three-Dimensional Turing Structures and Spatial Solitons in Optical Parametric Oscillators, *Phys. Rev. Lett.* **81**, 81 (1998).
- [28] M. Tlidi and P. Mandel, Three-Dimensional Optical Crystals and Localized Structures in Cavity Second Harmonic Generation, *Phys. Rev. Lett.* **83**, 4995 (1999).
- [29] I. Bordeu and M. G. Clerc, Rodlike localized structure in isotropic pattern-forming systems, *Phys. Rev. E* **92**, 042915 (2015).
- [30] S. S. Gopalakrishnan, K. Panajotov, M. Taki, and M. Tlidi, Dissipative Light Bullets in Kerr Cavities: Multistability, Clustering, and Rogue Waves, *Phys. Rev. Lett.* **126**, 153902 (2021).
- [31] Y. Pomeau, Front motion, metastability and subcritical bifurcations in hydrodynamics, *Phys. D (Amsterdam, Neth.)* **23**, 3 (1986).
- [32] I. Bordeu, M. G. Clerc, R. Lefever, and M. Tlidi, From localized spots to the formation of invaginated labyrinthine structures in a Swift-Hohenberg model, *Comm. Nonlinear Sci. Numer. Simulat.* **29**, 482 (2015).

# Supplementary Material on "Localized states with non-trivial symmetries: localized labyrinthine patterns"

M. G. Clerc,<sup>1</sup> S. Echeverría-Alar,<sup>1</sup> and M. Tlidi<sup>2</sup>

<sup>1</sup>*Departamento de Física and Millennium Institute for Research in Optics, Facultad de Ciencias Físicas y Matemáticas, Universidad de Chile, Casilla 487-3, Santiago, Chile*  
<sup>2</sup>*Département de Physique, Faculté des Sciences, Université Libre de Bruxelles (U.L.B.), CP 231, Campus Plaine, B-1050 Bruxelles, Belgium*

## I. LOCALIZED LABYRINTHINE PATTERNS

Labyrinthine patterns are disordered spatial structures characterized by a well-defined intrinsic length and presenting a powderlike ring spectrum in Fourier space [1], which signifies their lack of simple symmetry, local behavior of a single wavevector, and a large number of defects [2]. Localized labyrinthine patterns (LLP) arise as the stabilization of a labyrinthine pattern enclosed by a homogenous state. For example, they can be observed in the context of vegetation self-organization as irregular patches embedded in a uniform vegetated cover [cf. Fig. 1]. The localized vegetation labyrinths are robust and stationary, as shown in the temporal sequence of Figure 1, in which no relevant change is observed in a decade. Hence, natural systems can show the coexistence between states with trivial and nontrivial symmetries. Figure 2 shows stationary localized labyrinthine patterns obtained in different pattern forming models. The upper (lower) insets are the modulus of the global (averaged windowed) Fourier transform. From these Fourier transforms, one concludes that the localized patterns are disordered (upper insets) and locally characterized by a single mode (bottom insets).

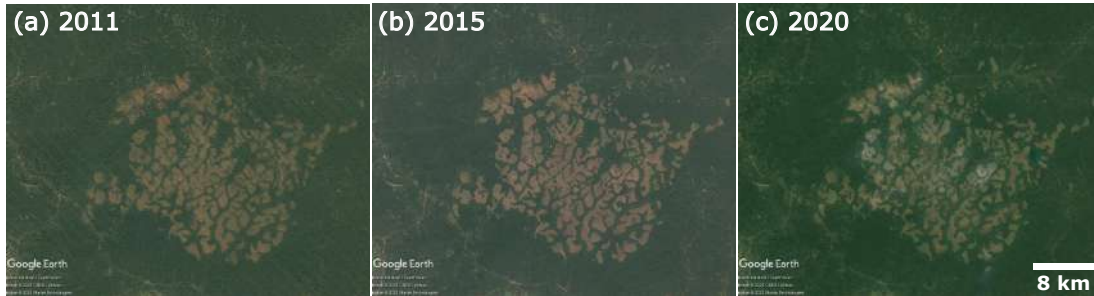


Figure 1: Temporal sequence of snapshots of a localized vegetation labyrinthine pattern. The localized labyrinthine pattern is observed in central Cameroon using Google Earth software (with ground coordinate 3°58'22.70" N 12°19'05.84" E [3]). The images were taken on December of (a) 2011, (b) 2015, and (c) 2020.

## II. SWIFT-HOHENBERG MODELS

To shed light in the existence, stabilization, and growth mechanisms of these new localized patterns, we consider the paradigmatic Swift-Hohenberg equation (SHE) [4]

$$\partial_t u = \epsilon u - u^3 - \nu \nabla^2 u - \nabla^4 u, \quad (1)$$

where  $u = u(x, y, t)$  is a real scalar field,  $\epsilon$  is the bifurcation parameter, and  $\nu > 0$  is the anti-diffusion coefficient, and a generalization version of the SHE [5, 6]

$$\partial_t u = \eta - \epsilon u - u^3 - (\nu - bu) \nabla^2 u - \nabla^4 u - c(\nabla u)^2, \quad (2)$$

where  $\epsilon$  and  $\eta$  are control parameters,  $\nu$ ,  $b$  are linear and nonlinear diffusion parameters, and  $c$  is the nonlinear advection strength. Both models support LLP [see Figs. 2(a) and 2(b)] in a pinning region where the uniform solutions  $u_{s\pm} = \pm\epsilon^{1/2}$  coexist with labyrinthine patterns of a critical wavelength  $\lambda_c = 2\sqrt{2\pi}/\sqrt{\nu}$ .

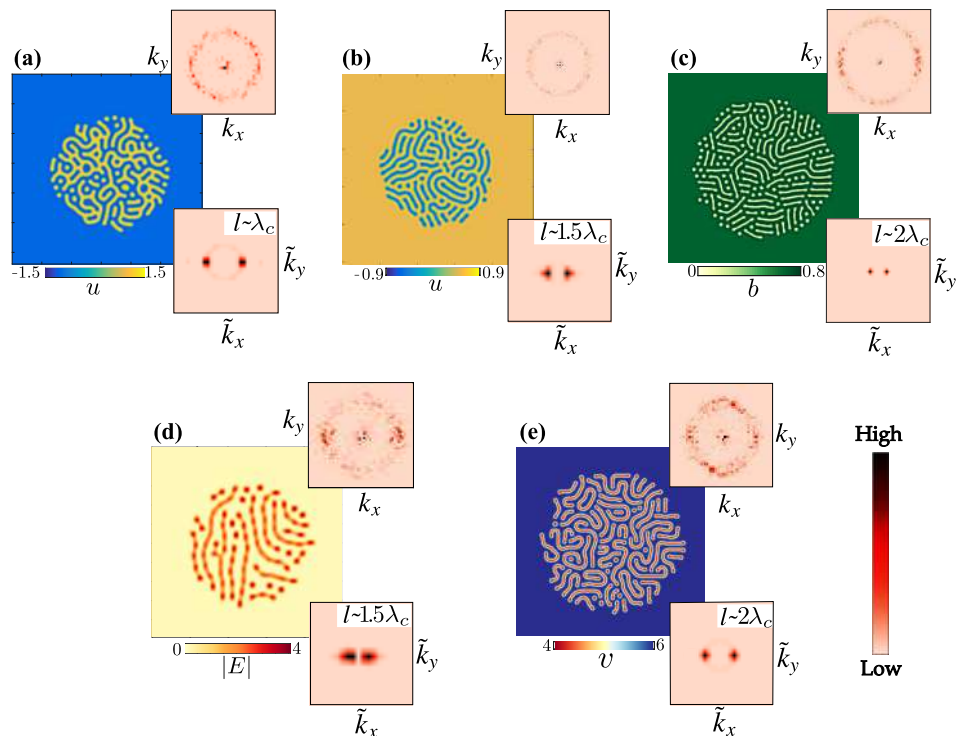


Figure 2: Stationary localized labyrinthine patterns obtained in different pattern forming models: (a) SHE (1) with  $\epsilon = 1.17$  and  $\nu = 1$ , (b) generalized SHE (2) with  $\epsilon = 0.2$ ,  $\nu = 1$ ,  $\eta = -0.06$ ,  $b = 0.1$ , and  $c = 0.1$ , (c) Non-local vegetation model Eq. (4) with  $L_f = 2.5$ ,  $D = 1$ ,  $\xi_f = 3$ ,  $\xi_c = 1$ ,  $\mu = 1.3$ , (d) Passive diffractive resonator equation (8) with  $C = 21$ ,  $\theta = -3.8$ , and  $E_i = 22$ , (e) reaction-diffusion model Eq. (10) with  $a = 17.16$ . The upper (lower) inset is the modulus of global (local) Fourier transform.  $\lambda_c$  and  $l$  are the critical wavelength ( $2\pi/|\vec{k}_c|$ ), of the corresponding model, and the size of the window in the averaged windowed Fourier transform, respectively.

30

### III. OTHER EXPERIMENTALLY RELEVANT SYSTEMS

31 The existence of stable localized labyrinthine structure is not limited to the large wavelength pattern regime  
 32 described by the paradigmatic Swift-Hohenberg equation but can be obtained from other experimentally relevant  
 33 systems. Three examples are chosen across various fields of natural science: (A) vegetation interaction-redistribution  
 34 model of vegetation dynamics, which can generate patterns even under strictly homogeneous and isotropic envi-  
 35 ronmental conditions. It is grounded on a spatially explicit formulation of the balance between facilitation and  
 36 competition. Ecosystems experience transitions towards fragmentation of landscapes followed by desertification con-  
 37 stitutes a major risk to the biological productivity of degraded zones, (B) nonlinear optical cavity subjected to a  
 38 coherent injected field, where localized states have been experimentally observed with a possibility for applications in  
 39 all-optical control of light, optical storage, and information processing, and (C) Chemical reaction-diffusion far from  
 40 equilibrium systems.

41

42

43

#### A. Vegetation interaction-redistribution model

44 The nonlocal approach, we adopt here focuses on the relationship between the structure of individual plants and the  
 45 facilitation-competition interactions existing within plant communities. Three types of interactions are considered: the  
 46 facilitative  $M_f(\vec{r}, t)$ , the competitive  $M_c(\vec{r}, t)$ , and the seed dispersion  $M_d(\vec{r}, t)$  nonlocal interactions. To simplify fur-  
 47 ther the mathematical modeling, we consider that the seed dispersion obeys a diffusive process  $M_d(\vec{r}, t) \approx D\nabla^2 b(\vec{r}, t)$ ,  
 48 where  $D$  is the diffusion coefficient. We assume in addition that all plants are mature neglecting the allometry, and they

are settled on flat territory  $\vec{r} = (x, y)$ , assuming isotropic environmental conditions. The interaction-redistribution model reads

$$M_i = \exp \left\{ \frac{\xi_i}{N_i} \int b(\vec{r} + \vec{r}', t) \phi_i(\vec{r}, t) d\vec{r}' \right\}, \text{ with } \phi_i(\vec{r}, t) = \exp(-\vec{r}/L_i) \quad (3)$$

where  $i = \{f, c\}$ .  $\xi_i$  represents the strength of the interaction,  $N_i$  is a normalization constant. We assume that their kernels  $\phi_i(\vec{r}, t)$  are exponential functions with  $L_i$  the range of their interactions.

A logistic equation with the above mentioned nonlocal interactions leads to the so called vegetation interaction-redistribution model. The spatiotemporal evolution of the normalized biomass density  $b(r, t)$  in isotropic environmental conditions reads [7]

$$\partial_t b(\vec{r}, t) = b(\vec{r}, t)[1 - b(\vec{r}, t)]M_f(\vec{r}, t) - \mu b(\vec{r}, t)M_c(\vec{r}, t) + DM_d(\vec{r}, t). \quad (4)$$

The normalization is performed with respect to the total amount of biomass supported by the system. The first two terms in the logistic equation with nonlocal interaction Eq. (4) describe the biomass gains and losses, respectively. The third term models seed dispersion. The aridity parameter  $\mu$  accounts for the biomass loss and gain ratio. Other approaches based on reaction-diffusion type of modelling incorporate water transport by below ground diffusion and/or above ground run-off [8].

The homogeneous steady state solutions of Eq. (4) are:  $b_o = 0$  which corresponds to the state totally devoid of vegetation, and the homogeneous cover solutions, which satisfy the equation

$$\mu = (1 - b) \exp \Delta b, \quad (5)$$

with  $\Delta = \xi_f - \xi_c$  measures the community cooperativity if  $\Delta > 0$  or anti-cooperativity when  $\Delta < 0$ . The bare state  $b_o = 0$  is unstable (stable)  $\mu < 1$  ( $\mu > 1$ ) and stable otherwise. The homogeneous cover state with higher biomass density is stable and the other is unstable. These solutions are connected by a saddle node or a tipping point whose coordinates are given by  $\{b_{sn} = (\Delta - 1)/\Delta, \mu_{sn} = e^{\Delta - 1}/\Delta\}$ . The linear stability analysis of the vegetated cover ( $b_s$ ) with respect to small fluctuations of the form  $b(\vec{r}, t) = b_s + \delta b \exp\{\sigma t + i\vec{k} \cdot \vec{r}\}$  with  $\delta b$  small, yields the dispersion relation

$$\sigma(k) = \left( b_s(1 - b_s)\xi_f - b_s - \frac{b_s(1 - b_s)\xi_c}{(1 + L_c^2 k^2)^{3/2}} \right) e^{\xi_f b_s} - Dk^2. \quad (6)$$

Given the spatial isotropy, the growth rate  $\sigma(k)$  is a real quantity. This eigenvalue may become positive for a finite band of unstable modes which triggered the spontaneous amplification of spatial fluctuations towards the formation of periodic structures with a well-defined wavelength ( $2\pi/k_c$ ). At the symmetry-breaking instability, the value of the critical wavenumber  $k_c$  marking the appearance of a band of unstable modes, and hence the symmetry-breaking instability, can be evaluated by two conditions:  $\sigma(k_c) = 0$  and  $\partial\sigma/\partial k|_{k_c} = 0$ . These conditions yield the most unstable mode

$$k_c^2 = \frac{1}{L_c^2} \left[ \left( \frac{3b_s e^{\xi_f b_s} (1 - b_s) \xi_c L_c^2}{2D} \right)^{2/5} - 1 \right]. \quad (7)$$

This critical wavenumber determines the wavelength of the periodic vegetation pattern  $2\pi/k_c$  that emerges from the symmetry-breaking instability. Replacing  $k_c$  in the condition  $\sigma(k_c) = 0$ , we can then calculate the critical biomass density  $b_c$ . The corresponding critical aridity parameter  $\mu_c$  is provided explicitly by the homogeneous steady states Eq. (5). The critical wavelength ( $2\pi/k_c$ ) determines the half space between stripes in the localized labyrinth, solution of Eq. (4), shown in Fig. 2.

## B. Passive nonlinear resonator model

We consider a passive resonator with plane mirrors, filled by a resonant two-level medium without population inversion and driven by a coherent plane-wave injected signal. In the good cavity limit where the medium relaxes much faster than the cavity field, the material variables (the atomic polarization and population difference) are

adiabatically eliminated, and the resulting model equation is a complex Ginzburg-Landau equation of the form

$$\partial_t E = E_i - (1 + i\theta)E - \frac{2CE}{1 + |E|^2} + i\nabla^2 E, \quad (8)$$

where  $E$  is the normalized slowly varying complex envelope of the electrical field circulating within the optical cavity,  $E_i$  is the input field amplitude,  $\theta$  is the detuning parameter, and  $C$  is a cooperative parameter. The homogenous steady state solutions ( $E_o$ ) satisfy

$$E_i^2 = \left\{ \left( 1 + \frac{2C}{1+I} \right)^2 + \theta^2 \right\} I, \quad (9)$$

where  $I = |E_o|^2$ . The emergence of bistability in the model can be established by the conditions  $d^2 E_i^2 / d^2 I = dE_i^2 / dI = 0$ . The system exhibits bistability if  $C > C_c$ , where  $C_c$  is solution of  $(C_c - 4)(1 + 2C_c^2) = 27\theta^2 C_c^2$ , with a critical cavity intensity  $I_c = (1 + 2C_c) / (C_c - 1)$ . The system exhibits two symmetry-breaking instabilities at  $I_T^\pm = C - 1 \pm \sqrt{C^2 - 4C}$ . The critical wavenumber at both instabilities is  $k_c = \sqrt{-\theta}$ . Close to this point a Swift-Hohenberg equation, Eq. (1), has been established [9]. The critical wavenumber defines a critical wavelength  $2\pi/k_c$ , which is the half space between the stripes observed in the localized labyrinthine pattern, solution of Eq. (8), shown in Fig. 2.

### C. Reaction-Diffusion model

Finally, reaction-diffusion systems are models of predilection for the study of dissipative structures and localized states. These models apply not only to chemical open reactors such as continuously stirred tank reactors (CSTR) but also to population dynamics such as population biology and epidemiology. In this context, the symmetry-breaking bifurcation is called the activation-inhibition instability. This bifurcation results from the competition between two opposite processes: a short-range positive feedback due to an activator that favours the growth of fluctuations and a long-range negative feedback due to an inhibitor that neutralizes the activator's action. We choose the Edblom, Orban, and Epstein (EOE) model [10].

$$\begin{aligned} \partial_t u &= -uv^2 + av - (1 + b)u + D\nabla^2 u \\ \partial_t v &= uv^2 - (1 + a)v + u + F + \nabla^2 v, \end{aligned} \quad (10)$$

where the dimensionless variables  $u$  and  $v$  corresponds to  $\text{HSO}_3$  and  $\text{H}^+$  concentrations, respectively.  $a$  and  $b$  are reduced reaction rates,  $d$  is the ratio of the diffusion constants of  $u$  and  $v$ , and  $F$  is the dimensionless inflow of hydrogen ions. The homogenous steady states of Eq. (10),  $u_o$  and  $v_o$ , are solutions of

$$\begin{aligned} u_o &= \frac{av_o}{v_o^2 + 1 + b} \\ \frac{av_o^3}{1 + b + v_o^2} - (1 + a)v_o + \frac{av_o}{1 + b + v_o^2} + F &= 0. \end{aligned} \quad (11)$$

In the case of  $b = 1$  and  $F = 7.65$  the system exhibits a S-shaped bifurcation diagram with  $a$  as the bifurcation parameter. The middle branch is always unstable. In the narrow range  $a \in [16.95, 17.04]$  the model displays bistability of homogenous states, characterized by a hysteresis loop. To characterize pattern formation in this chemical model we perform a linear stability analysis. We make perturbations of finite wavenumber around the stable homogenous states, i.e.

$$\begin{pmatrix} u(\vec{r}, t) \\ v(\vec{r}, t) \end{pmatrix} = \begin{pmatrix} u_o \\ v_o \end{pmatrix} + \begin{pmatrix} \delta u \\ \delta v \end{pmatrix} e^{i\vec{k}\cdot\vec{r} + \sigma t}. \quad (12)$$

After introducing Eq. (12) into Eq. (10), we obtain the linearized problem

$$\sigma \begin{pmatrix} \delta u \\ \delta v \end{pmatrix} = \begin{pmatrix} -v_o^2 - 1 - b - Dk^2 & -2u_o v_o + a \\ v_o^2 + 1 & 2u_o v_o - 1 - a - k^2 \end{pmatrix} \begin{pmatrix} \delta u \\ \delta v \end{pmatrix}. \quad (13)$$

111 We impose  $\sigma = \frac{\partial \sigma}{\partial k} = 0$  in the characteristic polynomial equation for  $\sigma$  and obtain the critical wavenumber,

$$k_c^2 = \frac{-v_c^2 - 1 - b + D(2u_c v_c - 1 - a_c)}{2D}, \quad (14)$$

112 together with Eq. (11) the critical point(s)  $(a_c, v_c)$  can be obtained. We find, numerically, that in the two stable  
 113 branches the Turing instability can arise. Note that, close to this critical point a non-variational Swift-Hohenberg  
 114 model (Eq. (2)) has been established [6]. Eq. (14) defines a critical wavelength  $2\pi/k_c$ , which is the half space between  
 115 stripes in the localized labyrinthine pattern in Fig. 2.

#### 116 IV. INITIAL AND BOUNDARY CONDITIONS, AND GRID INDEPENDENCE OF LOCALIZED 117 LABYRINTHINE PATTERNS

118 The nucleation process in the SHE model (1) is illustrated in Fig. 3. A circular patch of a diameter  $d$  is extracted  
 119 from the center of a stable labyrinthine pattern. Then, it is embedded in the uniform solution  $u_{s+}$  in order to create  
 120 the initial condition as shown in  $t_1$  in Fig. 3. The localized labyrinthine pattern evolves towards an equilibrium until  
 121 the temporal evolution of the Lyapunov Functional reaches a plateau, and the stable localized labyrinthine pattern  
 122 emerges. The step-like descend of the Lyapunov Functional at early stages of the temporal evolution is related to  
 123 the accomodation of defects in the frustrated labyrinthine pattern [2]. A similar procedure is used to generate the  
 124 three-dimensional LLP.

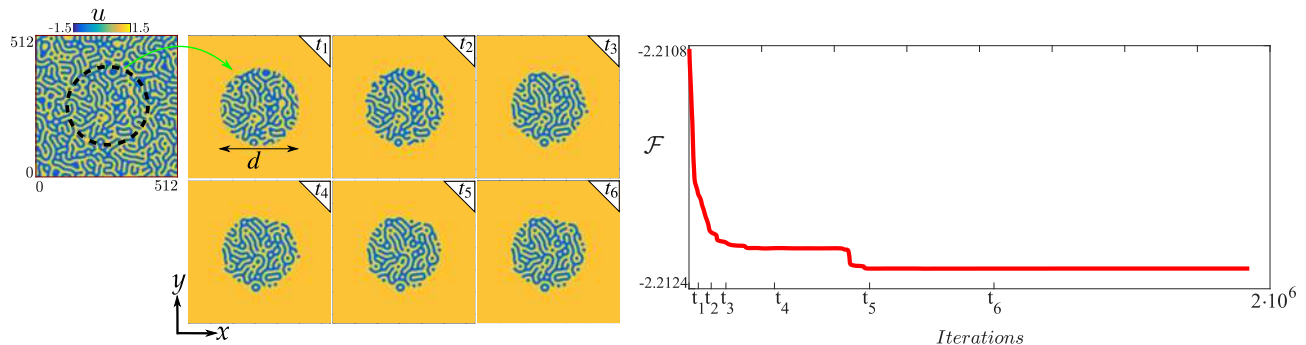


Figure 3: Creation and stabilization of a localized labyrinthine pattern in the SHE (1) with  $\epsilon = 1.165$  and  $\nu = 1$ . The left panel shows an extended labyrinthine pattern in equilibrium. The dashed circle indicates the patch of labyrinthine pattern that is embedded in the uniform solution. The size is  $d = 220$ . The middle panel accounts for the evolution towards equilibrium of the localized labyrinthine pattern ( $t_1 = 1$  to  $t_6 = 10^6$ , where  $t_1 < t_2 < t_3 < t_4 < t_5 < t_6$ ). The red curve in the right panel shows the minimization of the Lyapunov Functional  $\mathcal{F}$  during the stabilization of the localized labyrinthine pattern from the initial condition. See Supplementary Video 1 for the whole evolution.

127 In the SHE model (1), given an initial condition with a diameter  $d$ , LLP emerge as stable patterns when  $d \lesssim d_c$ .  
 128 Figure 4 shows the total area of localized labyrinthine patterns  $\|u\|^2$  for different initial conditions, considering the  
 129 same initial extended labyrinthine pattern. There is a transition between LLP and extended labyrinthine patterns  
 130 for  $d_c \approx 12\lambda_c$ . There is a finite size of stripes needed to localized the complex labyrinthine patterns. Also, there is a  
 131 minimum size  $d_o \approx 7\lambda_c$ , which gives the minimum amount of wavelengths to form a non-trivial symmetry pattern.

132 All the two-dimensional localized labyrinthine patterns shown in the main text and here [cf. Fig. 2 and Fig. 3]  
 133 are obtained using periodic boundary conditions. For completeness, we show that in the SHE model (1) the same  
 134 localized complex pattern can be seen in numerical simulations using Dirichlet and Neumann boundary conditions [see  
 135 Fig. 5]. All of these disordered localized patterns are obtained using the procedure described above. Also, we perform  
 136 numerical simulations in the SHE model (1) varying the numerical grid discretization,  $\Delta x$ , to show the numerical  
 137 robustness of LLP. These localized patterns are displayed in Fig. 6.

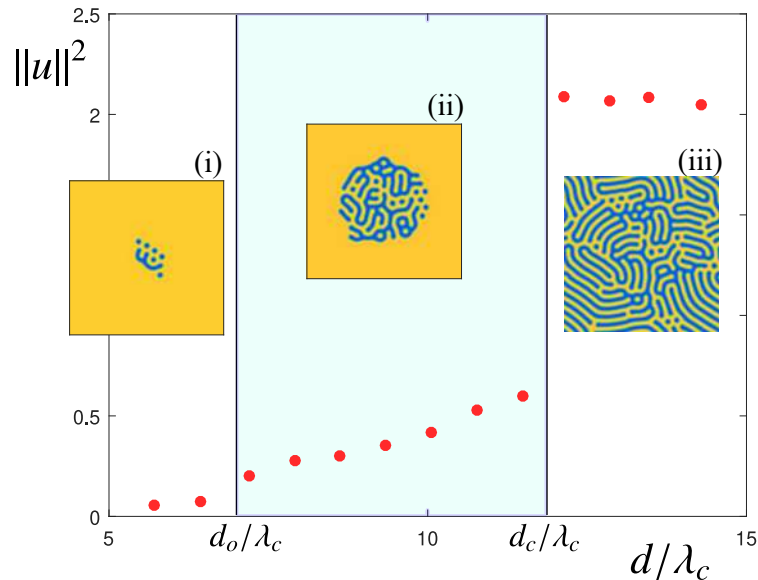


Figure 4: Transitions between (i) localized trivial symmetry patterns, (ii) localized non-trivial symmetry patterns, and (iii) extended labyrinthine patterns in the SHE model (1) with  $\epsilon = 1.164$  and  $\nu = 1$ .  $\|u\|^2$  is the area of the localized non-trivial symmetry patterns. The light blue shaded region accounts for the localized patterns with different degree of non-trivial symmetries exist.  $d_o \approx 7\lambda_c$  and  $d_c \approx 12\lambda_c$ .

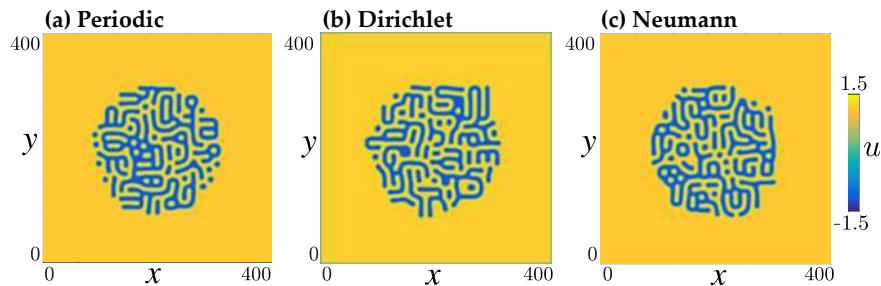


Figure 5: Different boundary conditions for the numerical simulations of localized labyrinthine patterns in the SHE (1) with  $\epsilon = 1.175$  and  $\nu = 1$ . Periodic (a), Dirichlet (b), and Neumann (c) boundary conditions. The diameter of the initial condition is  $d = 180$ .

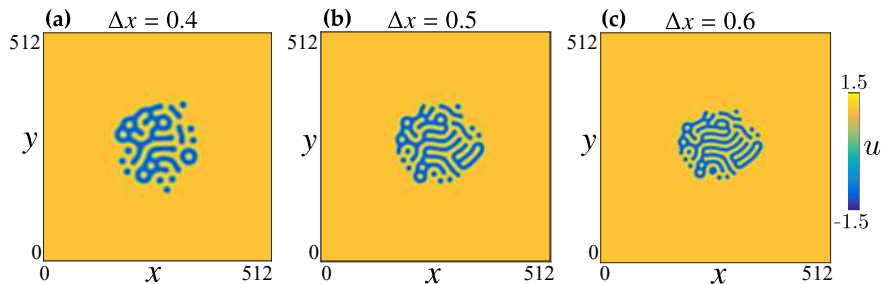


Figure 6: Localized labyrinthine patterns with different space discretizations  $\Delta x$  the SHE model (1) with  $\epsilon = 1.162$  and  $\nu = 1$ . (a)  $\Delta x = 0.4$ , (b)  $\Delta x = 0.5$ , and (c)  $\Delta x = 0.6$ . The initial diameter is  $d = 200$ .

138  
139

## V. GROWTH MECHANISM OF LOCALIZED LABYRINTHINE PATTERNS IN THE SWIFT-HOHENBERG EQUATION

140 Localized labyrinthine patterns, in the SHE model (1), are stable inside the pinning region delimited by  $\epsilon_p^-$  and  $\epsilon_p^+$   
141 as shown in Fig. 7, in which the square of the area supported by the localized labyrinthine patterns  $\|u\|^2$  is plotted  
142 as a function of the bifurcation parameter  $\epsilon$ . When varying  $\epsilon$  within this region, transitions between different LLP

143 are possible due to shrinking or expansion of fingers (at the interface or inside the labyrinthine structure), and the  
 144 accommodation of defects. Likewise, this shrinking process is accompanied by the appearance of circular spots and  
 145 the disappearance of local domains of stripe patterns. Figure 7 shows four LLP along one stable branch generated by  
 146 decreasing/increasing  $\epsilon$ , starting from  $\epsilon = \epsilon_{ic}$  [inset (i) in Fig. 7].

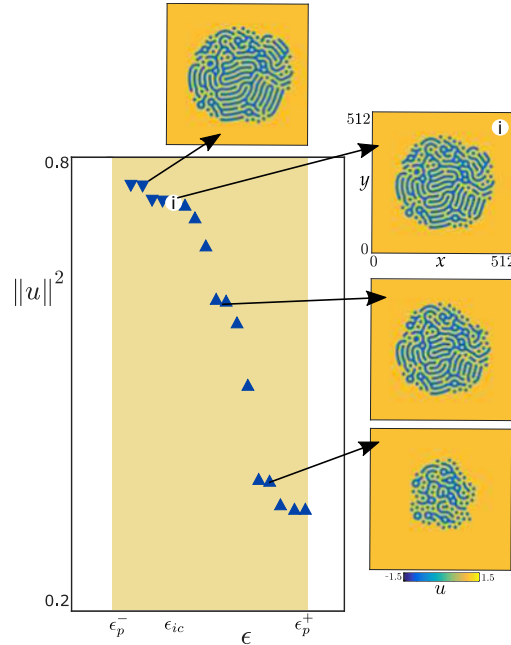


Figure 7: Localized labyrinthine patterns in the SHE model (1) along one stable branch (blue curve). The yellow shaded area with boundaries  $\epsilon_p^- = 1.16$  and  $\epsilon_p^+ = 1.19$  is the pinning region. Starting from the LLP in (i) at  $\epsilon_{ic} = 1.17$ , the bifurcation parameter is increased (upward triangles) and decreased (downward triangles).

- 
- 147 [1] M. Le Berre, E. Ressayre, A. Tallet, Y. Pomeau, and L. Di Menza, Example of a chaotic crystal: The labyrinth, Phys.  
 148 Rev. E **66**, 026203 (2002).  
 149 [2] S. Echeverria-Alar and M.G. Clerc, Labyrinthine patterns transitions, Phys. Rev. Research **2**, 042036(R) (2020).  
 150 [3] [https://earth.google.com/web/search/3+58%2722.70%22+N+12+19%2705.84%22+E/@4.01617577,](https://earth.google.com/web/search/3+58%2722.70%22+N+12+19%2705.84%22+E/@4.01617577,12.34456541,712.00876556a,54068.64445182d,35y,-24.30467639h,3.78631196t,-0r/data=CmAaNHlWGV1WF6alYA9AIRBcQMP2oihAKhwzIDU4JzIyLjcwIiB0IDEyIDE5JzA1LjgOIiBFGAIGASImCiQJRQp2zmWCDcARPzROa9_ADcAZXVIWd8BLPkAh6rEWsxw7PkA)  
 151 [12.34456541,712.00876556a,54068.64445182d,35y,-24.30467639h,3.78631196t,-0r/data=](https://earth.google.com/web/search/3+58%2722.70%22+N+12+19%2705.84%22+E/@4.01617577,12.34456541,712.00876556a,54068.64445182d,35y,-24.30467639h,3.78631196t,-0r/data=CmAaNHlWGV1WF6alYA9AIRBcQMP2oihAKhwzIDU4JzIyLjcwIiB0IDEyIDE5JzA1LjgOIiBFGAIGASImCiQJRQp2zmWCDcARPzROa9_ADcAZXVIWd8BLPkAh6rEWsxw7PkA)  
 152 [CmAaNHlWGV1WF6alYA9AIRBcQMP2oihAKhwzIDU4JzIyLjcwIiB0IDEyIDE5JzA1LjgOIiBFGAIGASImCiQJRQp2zmWCDcARPzROa9\\_](https://earth.google.com/web/search/3+58%2722.70%22+N+12+19%2705.84%22+E/@4.01617577,12.34456541,712.00876556a,54068.64445182d,35y,-24.30467639h,3.78631196t,-0r/data=CmAaNHlWGV1WF6alYA9AIRBcQMP2oihAKhwzIDU4JzIyLjcwIiB0IDEyIDE5JzA1LjgOIiBFGAIGASImCiQJRQp2zmWCDcARPzROa9_ADcAZXVIWd8BLPkAh6rEWsxw7PkA)  
 153 [ADcAZXVIWd8BLPkAh6rEWsxw7PkA](https://earth.google.com/web/search/3+58%2722.70%22+N+12+19%2705.84%22+E/@4.01617577,12.34456541,712.00876556a,54068.64445182d,35y,-24.30467639h,3.78631196t,-0r/data=CmAaNHlWGV1WF6alYA9AIRBcQMP2oihAKhwzIDU4JzIyLjcwIiB0IDEyIDE5JzA1LjgOIiBFGAIGASImCiQJRQp2zmWCDcARPzROa9_ADcAZXVIWd8BLPkAh6rEWsxw7PkA)  
 154 [4] J. Swift and P.C. Hohenberg, Hydrodynamic fluctuations at the convective instability, Phys. Rev. A **15**, 319 (1977).  
 155 [5] M.G. Clerc, A. Petrossian, and S. Residori, Bouncing localized structures in a liquid-crystal light-valve experiment, Phys.  
 156 Rev. E **71**, 015205 (2005).  
 157 [6] G. Kozyreff and M. Tlidi, Nonvariational real Swift-Hohenberg equation for biological, chemical, and optical systems,  
 158 Chaos **17**, 037103 (2007).  
 159 [7] M. Tlidi, *et al.* Lect. Notes Phys. **751**, 381 (2008).  
 160 [8] J. von Hardenberg, E. Meron, M. Shachak, and Y. Zarmi, Diversity of Vegetation Patterns and Desertification, Phys Rev  
 161 Lett **87** 198101 (2001).  
 162 [9] M. Le Berre, E. Ressayre, and A. Tallet, Why does a Ginzburg-Landau diffraction equation become a diffusion equation  
 163 in the passive ring cavity?, A. Quantum Semiclass Opt **7**, (1995).  
 164 [10] E.C. Edblom, M. Orban, and I. R. Epstein, A New Iodate Oscillator: The Landolt Reaction with Ferrocyanide in a CSTR,  
 165 J. Am. Chem. Soc. **108**, 2826 (1986).